RESEARCH ARTICLE
SPACE PHYSICS: IONOSPHERIC PHYSICS

Earth and Planetary Physics
9: 1–9, 2025
doi: 10.26464/epp2024038

Effects of mesoscale gravity waves on sporadic E simulated by a one-dimensional dynamic model

Xu Zhou[1,2], ZeZhong Li[3], XinAn Yue[1,2*], and LiBo Liu[1,2]

[1]Key Laboratory of Earth and Planetary Physics/Heilongjiang Mohe National Geophysical Observatory/Beijing National Observatory of Space Environment, Institute of Geology and Geophysics, Chinese Academy of Sciences (CAS), Beijing 100029, China;

[2]College of Earth and Planetary Sciences, University of Chinese Academy of Sciences, Beijing 100049, China;

[3]CAS Center for Excellence in Comparative Planetology/CAS Key Laboratory of Geospace Environment/Mengcheng National Geophysical Observatory, University of Science and Technology of China, Hefei 230026, China

Key Points:

- A one-dimensional dynamic model with low numerical dissipation is developed to simulate the evolution of sporadic E (E_s) layers.
- Mesoscale gravity waves (GWs, periods <2 h) significantly affect the E_s layers above 100 km, but the effects are limited at lower altitudes.
- The effects of GWs on the E_s layers are complicated and include the reinforcement, diffusion, and driving of the wavelike vertical motion.

Citation: Zhou, X., Li, Z. Z., Yue, X. A., and Liu, L. B. (2025). Effects of mesoscale gravity waves on sporadic E simulated by a one-dimensional dynamic model. *Earth Planet. Phys.*, *9*(1), 1–9. http://doi.org/10.26464/epp2024038

Abstract: In addition to being driven by tidal winds, the sporadic E (E_s) layers are modulated by gravity waves (GWs), although the effects are not yet comprehensively understood. In this article, we discuss the effects of mesoscale GWs on the E_s layers determined by using a newly developed model, MISE-1D (one-dimensional Model of Ionospheric Sporadic E), with low numerical dissipation and high resolution. Driven by the wind fields resolved by the high-resolution version of the Whole Atmosphere Community Climate Model with thermosphere and ionosphere extension (WACCM-X), the MISE-1D simulation revealed that GWs significantly influence the evolution of the E_s layer above 100 km but have a very limited effect at lower altitudes. The effects of GWs are diverse and complex, generally including the generation of fluctuating wavelike structures on the E_s layer with frequencies similar to those of the GWs. The mesoscale GWs can also cause increases in the density of E_s layers, or they can disperse or diffuse the E_s layers and increase their thickness. In addition, the presence of GWs is a key factor in sustaining the E_s layers in some cases.

Keywords: sporadic E; ion tidal layer; gravity waves; numerical simulation

1. Introduction

Sporadic E (E_s) refers to the enhanced ionized layers at altitudes of ~95–130 km, which have frequently been observed by multiple measurements (e.g., Ogawa et al., 2002; Hysell et al., 2014; Yu BK et al., 2020). The presence of E_s layers in nature scatters radio propagation and thus has impacts on radio communication and modern navigation (Yue XA et al., 2016). A widely accepted view to explain the formation of E_s layers is the wind shear mechanism: the vertical shear of zonal and meridional winds causes long-lived ions (e.g., metallic ions) to converge (Haldoupis, 2011; Yamazaki et al., 2022; Qiu LH et al., 2023b). The zonal winds drive the ions across the geomagnetic fields and produce a vertical motion by the Lorentz force. The meridional winds drive ions along the magnetic lines and generate vertical field-aligned transport. The variability of the neutral winds at the heights of E_s layers is mainly influenced by the atmospheric tides. Consequently, the E_s layers predominantly descend with the tidal nodes and are thus known as tidal ion layers (Mathews, 1998).

In addition to tidal winds, the atmospheric gravity waves (GWs) play a substantial role in the mesosphere and thermosphere. Although most GWs dissipate and deposit their momentum fluxes into the mean flow around the mesopause (~80 km), a spectrum of GWs still appears at the heights of the E_s layers (Lu X et al., 2009). These short-period fluctuations perturb the descending phase of the tides, thus producing complex effects on the E_s layers. Huang CS and Kelley (1996) predicted that the E_s layers will become a large-scale wavelike structure under the modulation of GWs. Gravity waves with short vertical wavelengths could shear out multiple E_s layers (Didebulidze et al., 2020). Short-term GWs with longer wavelengths, as presented by Qiu LH et al. (2023a), can also significantly affect the E_s layers. The ion density may increase more than twofold, or the E_s layers may disperse or even

First author: X. Zhou, zx0601@mail.iggcas.ac.cn
Correspondence to: X. A. Yue, yuexinan@mail.iggcas.ac.cn
Received 31 MAR 2024; Accepted 19 MAY 2024.
First Published online 25 JUN 2024.

disappear. Those works gave us the first glimpse of how the GWs influence the E_s evolution. However, from the simulation perspective, many issues still need to be improved. The priority is that the numerical scheme needs to satisfy the requirement for dealing with the dynamic processes in the fine grids. To simulate such a thin thickness of E_s layers, the model should have better conservation and less dissipation. Otherwise, the numerical scheme will additionally introduce spurious diffusion. Although the presence of diffusion in nature is important to prevent the E_s layer from becoming too thin, the spurious diffusion attributable to the numerical scheme could lead to overestimation of the dispersion effect of GWs on the E_s layers or could provide additional ions for GWs to shear out secondary E_s layers above or below the peaks. Moreover, the mesoscale GWs induce dramatic changes in the vertical wind shear, so this fact requires robust model stability to handle the rapid changes of inflow and outflow on the grids. In this work, we develop a novel one-dimensional Model of Ionospheric Sporadic E (MISE-1D), which solves the dynamic processes in the evolution of E_s with low numerical dissipation and has strong stability.

To investigate the effects of mesoscale GWs (periods <2 h) on the E_s layers, a series of numerical experiments are performed under conditions with and without GWs. The specified neutral winds, including the resolved mesoscale GWs, are provided by the high-resolution version of the Whole Atmosphere Community Climate Model with thermosphere and ionosphere extension (WACCM-X; Liu HL et al., 2023, 2024). In the first step, we exclude physical diffusion to examine whether the GWs facilitate the diffusion of E_s layers or have other influences. In the next step, the ambipolar diffusion is introduced, and the aim is to investigate how strong the GW effects are compared with the ambipolar diffusion. Because the strength of GWs depends on the latitudes (Hoffmann et al., 2013; Miyoshi et al., 2014), we select two typical locations at mid- and low latitudes in China, Mohe (53.5°N, 122.3°E) and Sanya (18.3°N, 109.6°E). The selection of location also considers that the two sites have established a new lidar and a new incoherent scatter radar, respectively, both of which can measure the E_s layers with high spatiotemporal resolution (Yue XA et al., 2022a, 2022b; Zhou X et al., 2023; Chen FL et al., 2024). Our simulation work should therefore be a very useful complement to future observations.

This article is organized as follows: The MISE-1D is introduced in Section 2, including the numerical scheme and specific settings. The effects of mesoscale GWs on the evolution of E_s layers are presented in Section 3. Section 4 discusses the advantages and disadvantages of the present work and gives a brief perspective of future studies. A summary is given at the end.

2. Model Description

2.1 Numerical Scheme

The E_s layers are formed by wind shear, so the dynamic calculation is the most important issue. In this work, we adopt a numerical scheme that has low diffusion, which has been applied to the simulation of ionospheric spread F (Li ZZ et al., 2021, 2023) and the magnetosphere (Zhang BZ et al., 2019). The MISE-1D numerically solves the continuous equation of ions by the finite-volume method, which has better conservation than the finite-difference method. Given that the electrons are strongly magnetized at the heights of the E_s layers, the plasma motion is equal to the ion motion, and electrons follow the ions by Coulomb force to maintain plasma neutrality. The integral form of the governing equation can then be expressed as

$$\frac{\partial}{\partial t}\iiint N_{\rm i}\mathrm{d}V = -\oiint F_{\rm i}\mathrm{d}S, \tag{1}$$

where $N_{\rm i}$ is the density of the metallic ion, $\mathrm{d}V$ is the control volume, and $\mathrm{d}S$ is the surface area. The total fluxes $F_{\rm i} = C_{\rm i} + D_{\rm i}$ comprise the convection attributable to vertical ion motion ($C_{\rm i} = N_{\rm i}w_{\rm i}$) and diffusion ($D_{\rm i}$), both of which are defined as positive in the outflowing direction of the interface surface. The production and loss terms (e.g., chemical recombination or metallic influx from space) are neglected in this dynamic model. In this one-dimensional model, the influx and outflux in the horizontal direction are ignored. Changes in number density in a time step can then be discretized as

$$N_j^{n+1} - N_j^n = -\frac{\Delta t}{\Delta h}\left(F_{j+1/2}^{n+1/2} - F_{j-1/2}^{n+1/2}\right), \tag{2}$$

where we discard the subscript i because both number density and fluxes are referred to as ions. The replaced subscript j indicates the jth grid vertically, and superscript n means the nth time step. The time step (Δt) is not set to be a constant but depends on the Courant–Friedrichs–Lewy condition (CFL) condition. A CFL value ($w_{\rm i}\Delta t/\Delta h$) less than 0.25 is safe to ensure the model stability for the convection calculation. As shown in Equation (3), the corrector step is calculated after a predictor step ($F^{n+1/2}$), which is given by the Adams–Bashforth scheme with third-order accuracy:

$$F^{n+\frac{1}{2}} = \frac{15}{8}F^n - \frac{5}{4}F^{n-1} + \frac{3}{8}F^{n-2}. \tag{3}$$

Figure 1 schematically illustrates the procedures in the dynamic calculation of the MISE-1D model.

2.1.1 Convection

To solve the convection, the flux values at $j+1/2$ interfaces are reconstructed according to the seventh upwind scheme (Zhang BZ et al., 2019):

$$\begin{aligned} C_{j+\frac{1}{2}} = &-\frac{1}{140}C_{j-3} + \frac{5}{84}C_{j-2} - \frac{101}{420}C_{j-1} + \frac{319}{420}C_j + \\ &\frac{107}{420}C_{j+1} - \frac{19}{210}C_{j+2} + \frac{1}{105}C_{j+3}. \end{aligned} \tag{4}$$

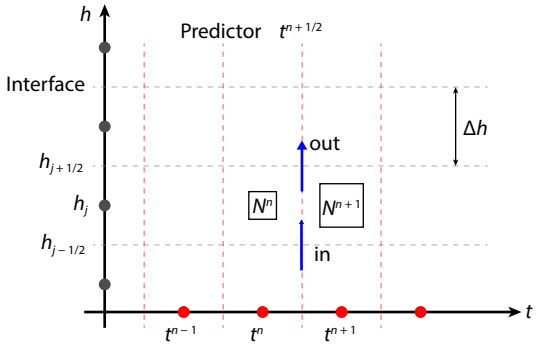

Figure 1. Schematic diagram of the numerical calculation procedures in the MISE-1D.

The flux values on the left and right sides utilize the same reconstruction coefficients by switching only the upwind direction. In addition, the limiter with the partial donor cell method is applied to monitor discontinuities. If the sharp discontinuities are captured, the limited values will be set to guarantee no overshooting or undershooting. The effective ion motion in vertical (w_i) is driven by the neutral winds, characterized as

$$w_i = \frac{\nu_{in}\omega_i}{\omega_i^2 + \nu_{in}^2} U\cos I - \frac{\omega_i^2}{\omega_i^2 + \nu_{in}^2} V\cos I\sin I = f_u U - f_v V, \tag{5}$$

where ν_{in} and ω_i are the ion-neutral collision frequency and gyrofrequency, respectively. The ion–ion and ion–electron collisions are ignored because of their small values in the region of interest. The calculation of the ion-neutral collision frequency requires information on the neutral temperature and the densities of nonmetallic species (e.g., O, O_2, N_2, NO), which, in this work, are provided by the NRLMSIS-00 model (Picone et al., 2002). The geomagnetic inclination I is given by the International Geomagnetic Reference Field (IGRF)-12 model (Thébault et al., 2015). The layer-forming efficiencies of zonal and meridional wind shear ($f_{u,v}$) are then calculated. The positive directions of zonal (U) and meridional (V) winds are eastward and northward, respectively. The effects of electric fields are not considered at present.

2.1.2 Diffusion

The metallic ions are the main constituents in the E_s layer, so they can be considered the major species. Although the molecular ions are also dominant in the daytime, the density of long-lived metallic ions is still large. The physical diffusion of major ion species in the vertical dimension is dominated by the ambipolar diffusion (Schunk and Nagy, 2009), which is written as

$$D_i = -\Gamma_a \left[\frac{\partial N_i}{\partial z} + \frac{N_i}{T_i + T_e} \frac{\partial (T_i + T_e)}{\partial z} - \frac{N_i m_i g \sin I}{k_B (T_i + T_e)} \right] \sin I, \tag{6}$$

where the ambipolar diffusion coefficient is given by

$$\Gamma_a = \frac{k_B (T_i + T_e)}{m_i \nu_{in}}. \tag{7}$$

The ion, electron, and neutral temperatures are assumed to be the same in this model ($T_e \simeq T_i \simeq T$) because of the sufficient heat exchanges between them in the E region. The calculation of the ion-neutral collision frequency (ν_{in}) adopts the formula in the SAMI3 (Sami3 is A Model of the Ionosphere) model (Huba et al., 2019). The k_B is the Boltzmann constant, and m_i is the ion mass density. Because the ambipolar diffusion is along the magnetic lines, the vertical motion attributable to diffusion should multiply the term of sin$I$. The discretization of ambipolar diffusion adopts an explicit scheme on the gradient terms based on the central difference method. The influx and outflux are calculated at the $j \pm 1/2$ interfaces of the predictor step. For example, changes in the density at the jth grid point caused by the diffusion of density gradients from time step n to time step $n+1$ are written as

$$\frac{\Delta t}{\Delta h^2} \left[\Gamma_{a_{j+\frac{1}{2}}}^{n+\frac{1}{2}} \left(N_{j+1}^{n+\frac{1}{2}} - N_j^{n+\frac{1}{2}} \right) - \Gamma_{a_{j-\frac{1}{2}}}^{n+\frac{1}{2}} \left(N_j^{n+\frac{1}{2}} - N_{j-1}^{n+\frac{1}{2}} \right) \right]. \tag{8}$$

Notably, to satisfy the stability requirement, the time step Δt in the diffusion calculation should at least be smaller than $\Delta h^2 / 2\Gamma_a$.

2.2 Model Settings

In this work, we choose the magnesium ion (Mg^+) for simulation, which is one of the most dominant metallic species in E_s layers. The initial profile of Mg^+ is given by the formula of Langowski et al. (2015):

$$N_{Mg^+} = \begin{cases} 10^9 \times \exp\left[-\dfrac{(h-97)^2}{60} \right] & (h < 97 \text{ km}) \\ 10^9 \times \exp\left[-\dfrac{(h-97)^2}{250} \right] & (h \geq 97 \text{ km}) \end{cases}, \tag{9}$$

where N_{Mg^+} is in m^{-3}, h is the altitude in units of kilometers.

The Mg^+ layer-forming efficiencies of zonal and meridional wind shear ($f_{u,v}$), which is mentioned in Equation (5), at the Mohe location are shown in Figure 2a. For the Mg^+ convergence, the meridional wind shear is more important than the zonal wind shear above ~120 km, and it increases with altitude. The zonal wind shear has

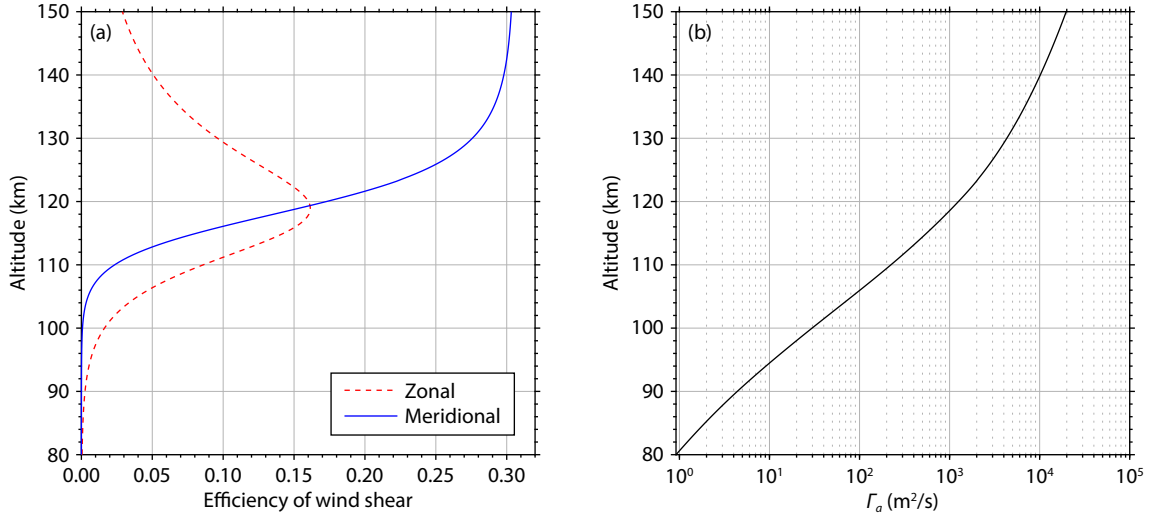

Figure 2. (a) Vertical profiles of Mg^+ layer-forming efficiencies of zonal (red dashed line) and meridional (blue solid line) wind shear. (b) Ambipolar diffusion coefficients of Mg^+ estimated as a function of altitude.

greater efficiency than the meridional wind shear below ~120 km, reaching a peak value of ~0.16. As for the ambipolar diffusion, the coefficients increase exponentially from 30 m^2/s at 100 km to ~20,000 m^2/s at 150 km (Figure 2b). This indicates that the diffusion in the upper E region is much stronger than that in the lower E region. We therefore set the height of the upper boundary at 150 km, rather than much higher, considering that the larger Γ_a at higher altitudes requires the time step to be extremely small.

Neutral winds are specified by the high-resolution version of the WACCM-X model (Liu HL et al., 2023), whose aim is to simulate the influences of the Hunga Tonga volcanic eruption in the atmosphere and ionosphere. The temporal resolution is 5 min and the vertical resolution at the height of E_s layers is ~0.6–2.0 km, so the model is able to capture the characteristics of mesoscale GWs (Liu HL et al., 2024). Figures 3a–3b show the resolved wind fields over Mohe (53.5°N, 122.3°E) at heights of 80–150 km. The semidiurnal tides are dominant at 80–100 km with a vertical wavelength of ~20 km. Gravity waves with smaller periods become much more important above 100 km. The mesoscale GWs are retrieved by high-pass filtering with a cutoff period of 2 h and are shown in Figures 3c–3d. The apparent period of the resolved mesoscale GWs is approximately 1.5 h, and the magnitude can reach ±50 m/s in the lower thermosphere (~100–150 km). The vertical wavelength of GWs above 100 km is approximately 30 km, and it increases with height. The wavefront of an apparent Lamb mode, which was generated by the Hunga Tonga volcanic eruption, reaches Mohe at approximately 16:00 universal time (UT), with a period of less than one hour. As for the horizontal winds over Sanya (Figure 4), diurnal tides dominate below 100 km, and semidiurnal tides become strong above 100 km. The amplitudes of GWs reach ~20 m/s, which are smaller than those at Mohe. The arrival time of the Lamb wave is ~14:00 UT, about 2 h earlier than that reaching Mohe.

3. Simulation Results

First, we examine the evolution of the Mg^+ density over Mohe simulated by the MISE-1D model, without the physical diffusion (Figure 5). Figures 5a–5b illustrate the results driven by the wind fields with and without the mesoscale GWs, respectively. The E_s layers above 100 km are thin in both the absence and presence of GWs, resulting from the exclusion of the diffusion term. The GWs mainly affect the E_s layers above 100 km, whereas their effects are much more limited below that. One of the most obvious effects is the short-period up-and-down motion. For instance, when the GWs are included, the peak height of the E_s layer decreases significantly from approximately 06:30 to 07:30 UT and fluctuates as the Lamb wave approaches (~16:00 UT). Another important influence is the strength of the E_s layer. The number density in the E_s layer above 100 km is much larger in the case with GWs than in the case without GWs. The GWs can also induce periodic changes in the E_s strength, which is strong at approximately 18:40, 20:10, and 21:40 UT. The time interval is similar to the wind period shown in Figure 3. In addition, GWs play a role in diffusing the E_s layer. The thin E_s layer begins to diffuse at ~120 km around 11:30 UT in the presence of GWs, whereas the E_s layer remains narrow at this time in the absence of GWs. Figure 6 further illustrates how the GWs disperse the E_s layer. The presence of GWs causes additional vertical wind shear in both the zonal and meridional winds, and the net effect is to induce additional upward ion motion above 120 km and downward ion motion below it. The different ion velocities at the interface of 120 km disperse the converged ion layer, and the net behavior is like diffusion. In this case, the full width at half maximum

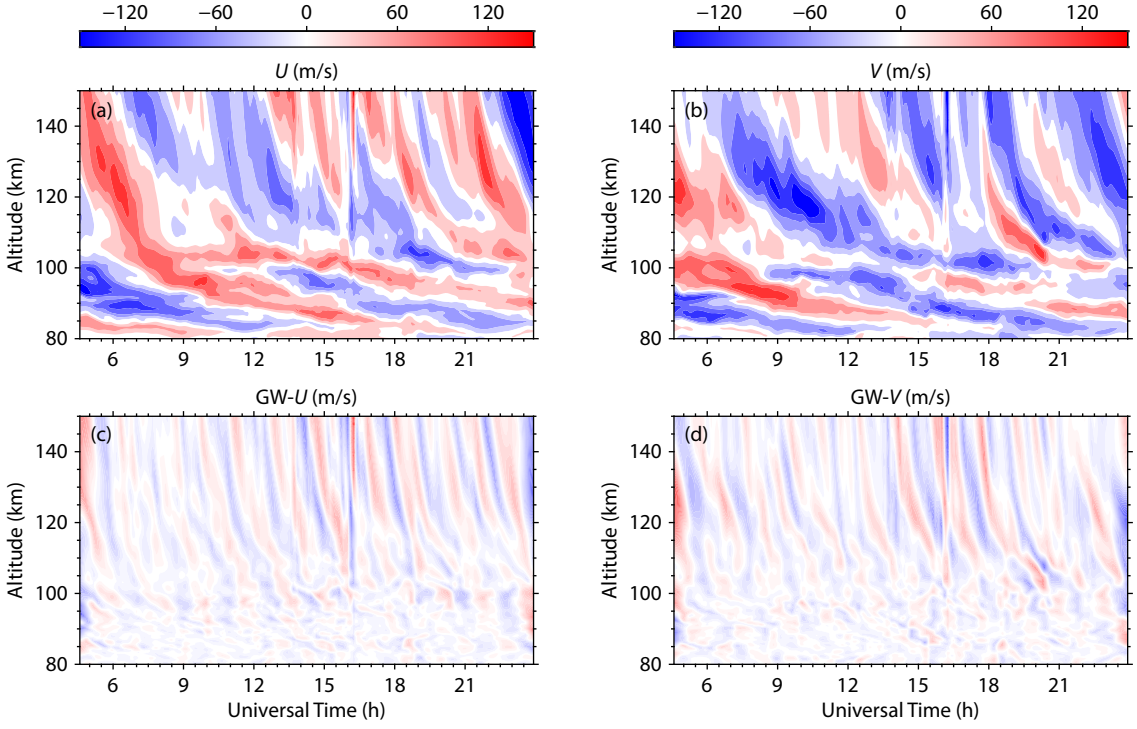

Figure 3. The (a) zonal (*U*) and (b) meridional (*V*) winds simulated by the high-resolution WACCM-X model on January 15, 2022, over Mohe (53.5°N, 122.3°E). Mesoscale gravity waves (GW; periods <2 h) are filtered from the simulated winds, as illustrated in plots (c) and (d).

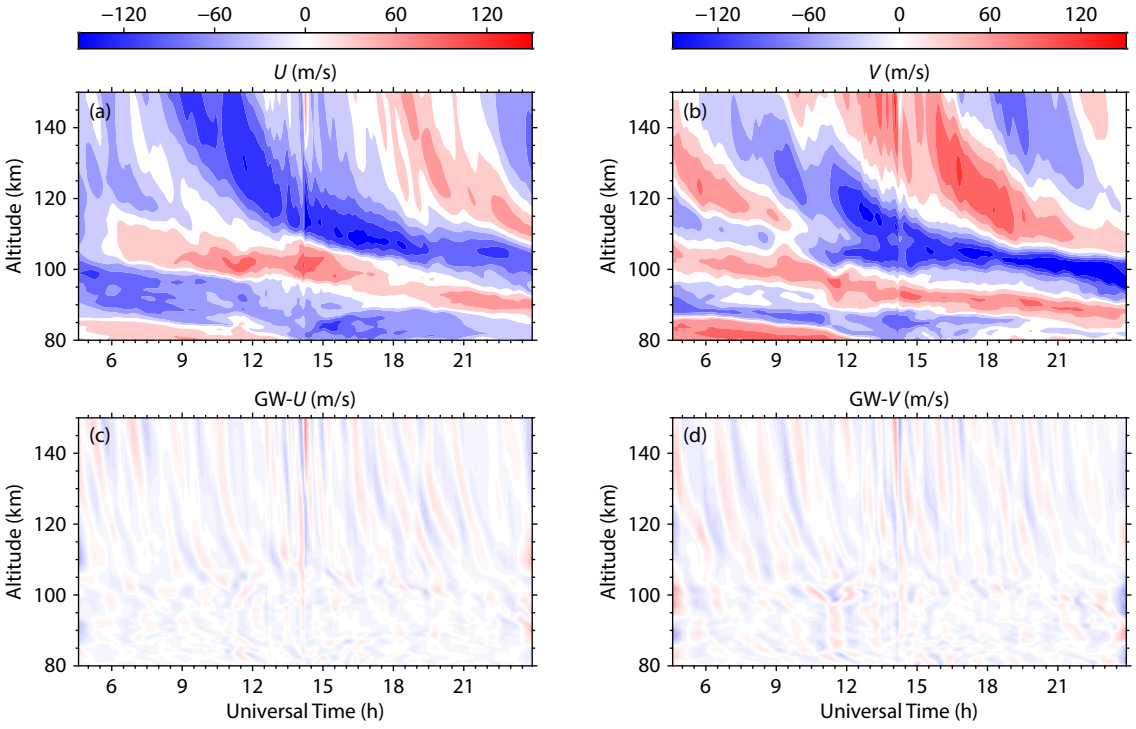

Figure 4. Same as Figure 3, but for the Sanya location (18.3°N, 109.6°E).

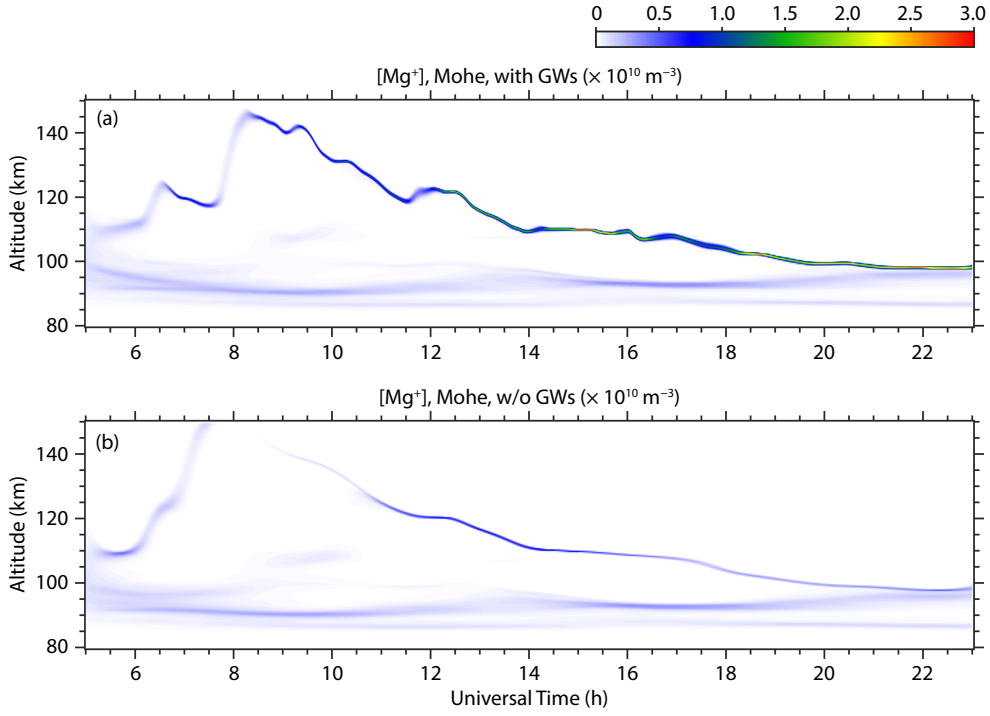

Figure 5. Temporal evolution of number density of Mg^+ (a) with and (b) without (abbreviated as w/o) the mesoscale GWs simulated under nondiffusion conditions.

(FWHM) of the E_s layer increases from ~0.8 to ~2.4 km because of the presence of GWs. In particular, the effects of GWs on E_s evolution are apparently complex, involving periodic up-and-down motions, an increase in density, and the diffusion of the E_s layers.

The ambipolar diffusion is then included in the MISE-1D simulation (Figure 7). The Mg^+ density is generally much lower and the thickness of the E_s layers is larger than that without diffusion (Figure 5), especially above 120 km, where the diffusion coefficient becomes large. The MISE-1D model captures the reasonable FWHM of the E_s layers (~1–5 km), which is comparable with that in the observation (Qiu LH et al., 2021). The effects of GWs on the E_s layers are similar to those without ambipolar diffusion, which also manifests

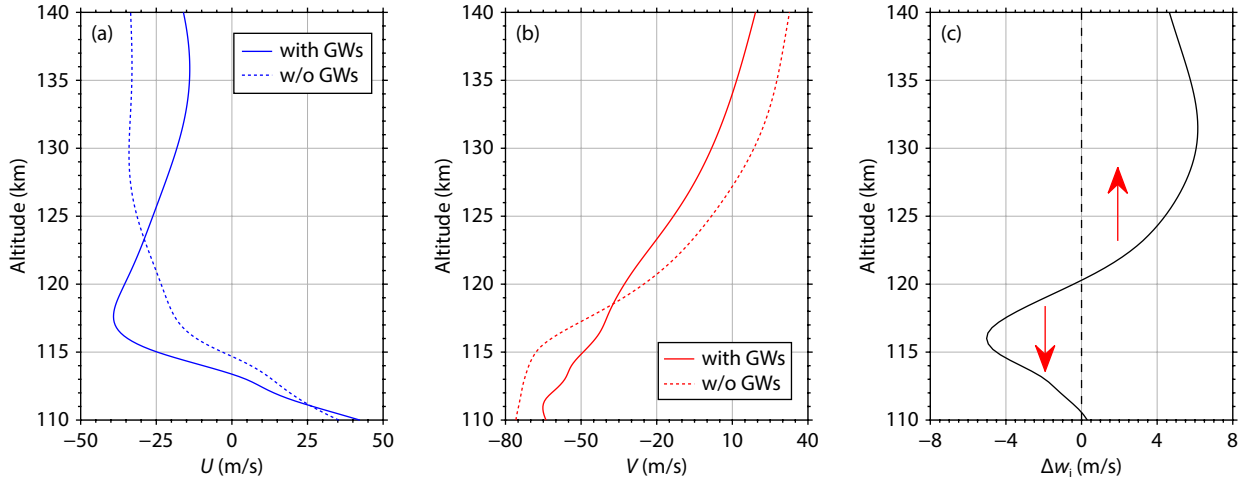

Figure 6. Vertical profiles of (a) zonal (*U*) and (b) meridional (*V*) winds in the presence (solid lines) and absence (dotted lines) of mesoscale GWs, at 11:30 UT. The corresponding differences in gyrofrequency (w_i) are plotted in panel (c), where red arrows indicate the direction of ion motion attributable to the GW effects.

as an up-and-down fluctuation, reinforcement, and dispersion of the E_s layers. However, in contrast to the report by Didebulidze et al. (2020), no significant multilayer effect is observed. This may be partly because the WACCM-X resolved the wavelength of mesoscale GWs in the lower thermosphere as larger than that specified by Didebulidze et al. (2020). Although the wavelengths of GWs below 100 km in this work are similar to those in their work, the GW effects at these altitudes in our simulation are still nonsignificant. In addition, the GWs in this case can generate a similar magnitude of dispersion on E_s layers compared with ambipolar diffusion, for example, around 11:50 and 16:40 UT.

In addition, Figure 8 shows the simulation results at Sanya without the consideration of ambipolar diffusion. This plot is intended to illustrate the effects of GWs alone rather than as a comparison between the effects of GWs and ambipolar diffusion. In the absence of GWs, the intensity of the E_s layer above 100 km is much weaker than that over Mohe and even disappears after 14:00 UT, although the vertical wind shear is also very strong (Figure 4). This result is consistent with our intuition because the geomagnetic inclination at Sanya is relatively small (~25.7°), which prevents the ions from converging vertically. As a result, the occurrence of the E_s layer at low latitudes is much smaller than that at mid-latitudes (Yu BK et al., 2019; Liu Y., 2021). However, once the GWs are included, the E_s layer over Sanya becomes as strong as that over Mohe. With the arrival of the Lamb wave

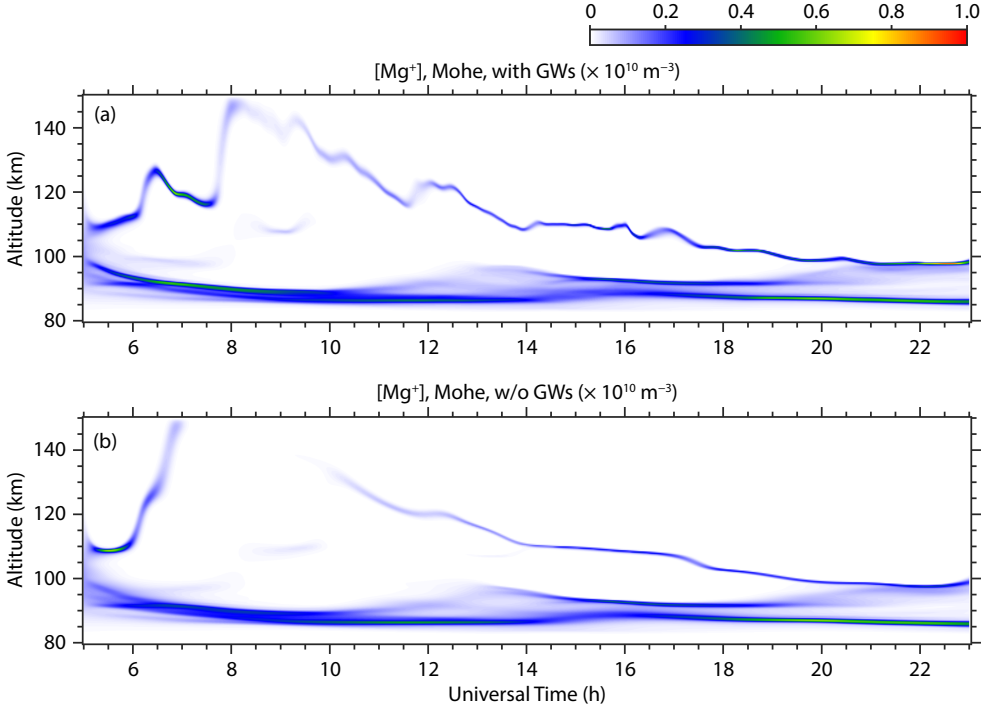

Figure 7. Same as Figure 5, but with consideration of the ambipolar diffusion.

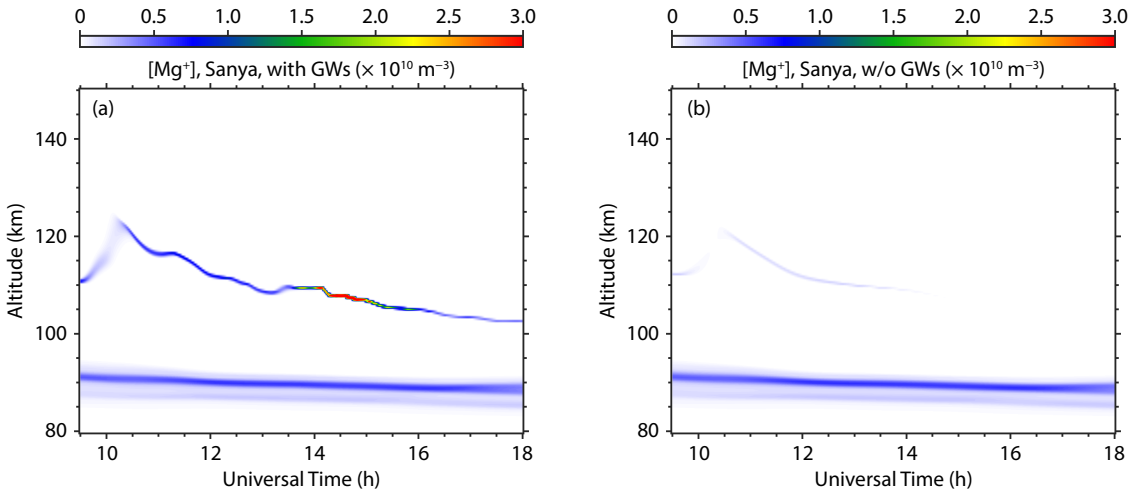

Figure 8. The evolution of E_s layers over Sanya in the (a) presence and (b) absence of mesoscale GWs without the ambipolar diffusion.

around 14:00 UT, the E_s layer is significantly strengthened and continuously maintained. The GWs also affect the E_s layer over Sanya similar to that over Mohe, for example, by generating fluctuation and increasing its thickness. But in this case, the mesoscale GWs are also a key factor in maintaining the E_s layer.

4. Discussion

One of the advantages of this work is the numerical scheme in the convection calculation, which has low dissipation and can simulate rapid changes in the evolution of the E_s layer with high resolution. Low dissipation is also advantageous for discussing the GW diffusion effect compared with physical diffusion in nature. Physical diffusion is crucial for the evolution of E_s layers, especially in the upper E region, where ion-neutral collisions decrease. The presence of physical diffusion prevents the E_s layer from becoming too narrow and maintains a thickness of approximately 1–5 km (Qiu LH et al., 2021). In addition, physical diffusion is thought to contribute to the disappearance of the E_s layers (Earle et al., 2000). Neglecting the physical diffusion term has been a common treatment in previous simulation studies, and their models have still been able to simulate E_s layers with a reasonable thickness (e.g., Zuo XM et al., 2006; Carrasco et al. 2007). Ignoring physical diffusion has generally not been very problematic because the numerical schemes generally introduce additional numerical dissipation, which is actually helpful in maintaining model stability. The numerical dissipation also acts as spurious diffusion to spread the E_s layers and prevent the layers from becoming too thin. However, numerical dissipation mostly depends on the calculation scheme, whereas diffusion in nature varies with height. When we discuss the possible roles of GWs in the diffusion or dispersion of E_s layers, the conventional treatment in the numerical scheme needs to be reconsidered, and adoption of a scheme with low numerical dissipation is necessary.

We found that the mesoscale GWs could dynamically disperse the E_s layers as strongly as the physical ambipolar diffusion, benefiting from the numerical consideration. When the vertical shear of the GWs induced the parting motion around the E_s peaks in the opposite direction, the E_s layer would disperse and the thickness would become greater. However, the effect of the dynamic diffusion mechanism on the terrestrial E_s layers would not produce the E_s "rifts" similar to those constantly observed on Mars (Collinson et al., 2020). In our simulation, the GWs did not form multiple E_s layers, as reported by Didebulidze et al. (2020). The compelling reason for this difference is that the wavelength they artificially specified was as short as 15 km, whereas the WACCM-X resolved the wavelength of GWs in the E_s heights as being larger than 30 km above 100 km. Although ambipolar diffusion was involved, the GWs still did not shear additional E_s layers. Moreover, the GW wavelengths in the simulation by Qiu LH et al. (2023a) were quite large, and they also did not find multiple layering effects.

The MISE-1D at the current stage is a simple convection–diffusion model. The consideration of GW influences in this work is only from a dynamical perspective, and chemical reactions and electric fields are not considered, some aspects of which are also important (Andoh et al., 2022, 2023). It would be worthwhile to include these processes and develop a three-dimensional framework in future research. In addition, with the progress of observations, fine structures inside the E_s layer have gradually been revealed (e.g., Hysell et al., 2013; Ejiri et al., 2019; Jiao J et al., 2022). These small-scale structures are thought to be associated with plasma instabilities, such as the Kelvin–Helmholtz instability (e.g., Larsen, 2000; Bernhardt, 2002), the gradient-drift instability (Woodman et al., 1991), and the GW-driven plasma instability (Shalimov et al., 2009). Some simulation work has resulted in preliminary discussions of these nonlinear processes (e.g., Cosgrove and Tsunoda, 2003; Wu JN et al., 2022), and more extensive discussions coupling advanced simulations and observations would deepen our understanding.

5. Conclusions

In this work, we developed a novel dynamic model, MISE-1D, to simulate the effects of GWs on the evolution of E_s layers. The model calculated the metallic-ion motion in the vertical direction based on the finite-volume method, with careful consideration of the numerical dissipation. Neutral winds simulated by the high-resolution version of WACCM-X were then specified in the model, and the effects of mesoscale GWs (periods <2 h) were evaluated. When the simulation results with and without the mesoscale GWs were compared, the effects of GWs on the E_s layers were revealed

and were found to be significant above 100 km. These effects were generally diverse and complicated for both the Mohe and Sanya sites. Such effects included the generation of wavelike fluctuations, the enhancement of strength, and the dispersion of E_s layer thickness. This dynamic dispersion effect is comparable with ambipolar diffusion at ~120 km. The presence of GWs can also be a critical factor in maintaining the E_s layers in certain cases.

Acknowledgments

This work was supported by the Project of Stable Support for Youth Teams in Basic Research Field, Chinese Academy of Sciences (CAS; Grant No. YSBR-018), the B-type Strategic Priority Program of CAS (Grant No. XDB41000000), the National Natural Science Foundation of China (Grant No. 42204165), and the National Key Research and Development Program (Grant No. 2022YFF0504400). The neutral wind simulated by the high-resolution WACCM-X model used for this study is available through Globus (globus.org), with the shared endpoint at https://tinyurl.com/3hnwjz93.

References

Andoh, S., Saito, A., and Shinagawa, H. (2022). Numerical simulations on day-to-day variations of low-latitude E_s layers at Arecibo. *Geophys. Res. Lett.*, *49*(7), e2021GL097473. https://doi.org/10.1029/2021GL097473

Andoh, S., Saito, A., and Shinagawa, H. (2023). Simulation of horizontal sporadic E layer movement driven by atmospheric tides. *Earth Planets Space*, *75*(1), 86. https://doi.org/10.1186/s40623-023-01837-0

Bernhardt, P. A. (2002). The modulation of sporadic-E layers by Kelvin–Helmholtz billows in the neutral atmosphere. *J. Atmos. Solar-Terr. Phys.*, *64*(12-14), 1487–1504. https://doi.org/10.1016/S1364-6826(02)00086-X

Carrasco, A. J., Batista, I. S., and Abdu, M. A. (2007). Simulation of the sporadic *E* layer response to prereversal associated evening vertical electric field enhancement near dip equator. *J. Geophys. Res.: Space Phys.*, *112*(A6), A06324. https://doi.org/10.1029/2006JA012143

Chen, F. L., Xun, Y. C., Wang, Z. L., Du, L. F., Zheng, H. R., Chen, Z. Q., Cheng, X. W., Wang, J. Q., Wu, F., and Yang, G. T. (2024). Preliminary results of calcium atom analysis by the wind–temperature–metal constituents LiDAR at Mohe middle-upper atmosphere for the Phase II of Chinese Meridian Project. *Rev. Geophys. Planet. Phys. (in Chinese)*, *55*(1), 131–137. https://doi.org/10.19975/j.dqyxx.2023-012

Collinson, G. A., McFadden, J., Grebowsky, J., Mitchell, D., Lillis, R., Withers, P., Vogt, M. F., Benna, M., Espley, J., and Jakosky, B. (2020). Constantly forming sporadic E-like layers and rifts in the Martian ionosphere and their implications for Earth. *Nat. Astron.*, *4*(5), 486–491. https://doi.org/10.1038/s41550-019-0984-8

Cosgrove, R. B., and Tsunoda, R. T. (2003). Simulation of the nonlinear evolution of the sporadic-*E* layer instability in the nighttime midlatitude ionosphere. *J. Geophys. Res.*, *108*(A7), 1283. https://doi.org/10.1029/2002JA009728

Didebulidze, G. G., Dalakishvili, G., and Todua, M. (2020) Formation of multilayered sporadic E under an influence of atmospheric gravity waves (AGWs). *Atmosphere, 11*(6), 653. https://doi.org/10.3390/atmos11060653

Earle, G. D., Bishop, R. L., Collins, S. C., González, S. A., and Sulzer, M. P. (2000). Descending layer variability over Arecibo. *J. Geophys. Res.: Space Phys.*, *105*(A11), 24951–24961. https://doi.org/10.1029/2000JA000029

Ejiri, M. K., Nakamura, T., Tsuda, T. T., Nishiyama, T., Abo, M., Takahashi, T., Tsuno, K., Kawahara, T. D., Ogawa, T., and Wada, S. (2019). Vertical fine structure and time evolution of plasma irregularities in the E_s layer observed by a high-resolution Ca^+ lidar. *Earth Planets Space*, *71*(1), 3. https://doi.org/10.1186/s40623-019-0984-z

Haldoupis, C. (2011). A tutorial review on sporadic *E* layers. In M. A. Abdu, et al. (Eds.), *Aeronomy of the Earth's Atmosphere and Ionosphere*. Dordrecht, Netherlands: Springer. https://doi.org/10.1007/978-94-007-0326-1_29

Hoffmann, L., Xue, X., and Alexander, M. J. (2013). A global view of stratospheric gravity wave hotspots located with Atmospheric Infrared Sounder observations. *J. Geophys. Res.: Atmos.*, *118*(2), 416–434. https://doi.org/10.1029/2012JD018658

Huang, C. S., and Kelley, M. C. (1996). Numerical simulations of gravity wave modulation of midlatitude sporadic *E* layers. *J. Geophys. Res.: Space Phys.*, *101*(A11), 24533–24543. https://doi.org/10.1029/96JA02327

Huba, J. D., Krall, J., and Drob, D. (2019). Global ionospheric metal ion transport with SAMI3. *Geophys. Res. Lett.*, *46*(14), 7937–7944. https://doi.org/10.1029/2019gl083583

Hysell, D. L., Nossa, E., Aveiro, H. C., Larsen, M. F., Munro, J., Sulzer, M. P., and González, S. A. (2013). Fine structure in midlatitude sporadic *E* layers. *J. Atmos. Solar-Terr. Phys.*, *103*, 16–23. https://doi.org/10.1016/j.jastp.2012.12.005

Hysell, D. L., Munk, J., and McCarrick, M. (2014). Sporadic *E* ionization layers observed with radar imaging and ionospheric modification. *Geophys. Res. Lett.*, *41*(20), 6987–6993. https://doi.org/10.1002/2014GL061691

Jiao, J., Chu, X. Z., Jin, H., Wang, Z. L., Xun, Y. C., Du, L. F., Zheng, H. R., Wu, F. J., Xu, J. Y., … Yang, G. T. (2022). First lidar profiling of meteoric Ca^+ ion transport from ~80 to 300 km in the midlatitude nighttime ionosphere. *Geophys. Res. Lett.*, *49*(18), e2022GL100537. https://doi.org/10.1029/2022GL100537

Langowski, M. P., von Savigny, C., Burrows, J. P., Feng, W., Plane, J. M. C., Marsh, D. R., Janches, D., Sinnhuber, M., Aikin, A. C., and Liebing, P. (2015). Global investigation of the Mg atom and ion layers using SCIAMACHY/Envisat observations between 70 and 150 km altitude and WACCM-Mg model results. *Atmos. Chem. Phys.*, *15*, 273–295 https://doi.org/10.5194/acp-15-273-2015, 2015

Larsen, M. F. (2000). A shear instability seeding mechanism for quasiperiodic radar echoes. *J. Geophys. Res.: Space Phys.*, *105*(A11), 24931–24940. https://doi.org/10.1029/1999JA000290

Li, Z. Z., Lei, J. H., and Zhang, B. Z. (2021). Numerical considerations in the simulation of equatorial spread F. *J. Geophys. Res.: Space Phys.*, *126*(10), e2021JA029622. https://doi.org/10.1029/2021JA029622

Li, Z. Z., Lei, J. H., and Zhang, B. Z. (2023). Three-dimensional simulation of equatorial spread F: effects of field-aligned plasma flow and ionospheric conductivity. *J. Geophys. Res.: Space Phys.*, *128*(3), e2022JA031070. https://doi.org/10.1029/2022JA031070

Liu, H. L., Wang, W., Huba, J. D., Lauritzen, P. H., and Vitt, F. (2023). Atmospheric and ionospheric responses to Hunga-Tonga volcano eruption simulated by WACCM-X. *Geophys. Res. Lett.*, *50*(10), e2023GL103682. https://doi.org/10.1029/2023GL103682

Liu, H. L., Lauritzen, P. H., and Vitt, F. (2024). Impacts of gravity waves on the thermospheric circulation and composition. *Geophys. Res. Lett.*, *51*(3), e2023GL107453. https://doi.org/10.1029/2023GL107453

Liu, Y., Zhou, C., Xu, T., Tang, Q., Deng, Z. X., Chen, G. Y., and Wang, Z. K. (2021). Review of ionospheric irregularities and ionospheric electrodynamic coupling in the middle latitude region. *Earth Planet. Phys.*, *5*(5), 462–482. https://doi.org/10.26464/epp2021025

Lu, X., Liu, A. Z., Swenson, G. R., Li, T., Leblanc, T., and McDermid, I. S. (2009). Gravity wave propagation and dissipation from the stratosphere to the lower thermosphere. *J. Geophys. Res.: Atmos.*, *114*(D11), D11101. https://doi.org/10.1029/2008JD010112

Mathews, J. D. (1998). Sporadic E: current views and recent progress. *J. Atmos. Solar-Terr. Phys.*, *60*(4), 413–435. https://doi.org/10.1016/S1364-6826(97)00043-6

Miyoshi, Y., Fujiwara, H., Jin, H., and Shinagawa, H. (2014). A global view of gravity waves in the thermosphere simulated by a general circulation model. *J. Geophys. Res.: Space Phys.*, *119*(7), 5807–5820. https://doi.org/10.1002/2014JA019848

Ogawa, T., Takahashi, O., Otsuka, Y., Nozaki, K., Yamamoto, M., and Kita, K. (2002). Simultaneous middle and upper atmosphere radar and ionospheric sounder observations of midlatitude *E* region irregularities and sporadic *E* layer. *J. Geophys. Res.: Space Phys.*, *107*(A10), SIA 3-1-SIA 3-13.

https://doi.org/10.1029/2001JA900176

Picone, J. M., Hedin, A. E., Drob, D. P., and Aikin, A. C. (2002). NRLMSISE-00 empirical model of the atmosphere: statistical comparisons and scientific issues. *J. Geophys. Res.: Space Phys., 107*(A12), SIA 15-1–SIA 15-16. https://doi.org/10.1029/2002ja009430

Qiu, L. H., Yu, T., Yan, X. X., Sun, Y. Y., Zuo, X. M., Yang, N., Wang, J., and Qi, Y. F. (2021). Altitudinal and latitudinal variations in ionospheric sporadic-E layer obtained from FORMOSAT-3/COSMIC radio occultation. *J. Geophys. Res.: Space Phys.*, *126*(9), e2021JA029454. https://doi.org/10.1029/2021JA029454

Qiu, L. H., Yamazaki, Y., Yu, T., Becker, E., Miyoshi, Y., Qi, Y. F., Siddiqui, T. A., Stolle, C., Feng, W. H., … Liu, H. X. (2023a). Numerical simulations of metallic ion density perturbations in sporadic E layers caused by gravity waves. *Earth Space Sci.*, *10*(8), e2023EA003030. https://doi.org/10.1029/2023EA003030

Qiu, L. H., Lu, X., Yu, T., Yamazaki, Y., Liu, H. X., Sun, Y.-Y., Wu, H. N., Zuo, X. M., Yan, X. X., Yu, Y., and Qi, Y. F. (2023b). Horizontal structure of convergent wind shear associated with sporadic E layers over East Asia. *Earth Planet. Phys.*, *7*(5), 548–557. https://doi.org/10.26464/epp2023071

Schunk, R., and Nagy, A. (2009). *Ionospheres: Physics, Plasma Physics, and Chemistry* (2nd ed). Cambridge, UK: Cambridge University Press. https://doi.org/10.1017/CBO9780511635342

Shalimov, S., Ogawa, T., and Otsuka, Y. (2009). On the gravity wave-driven instability of E layer at mid-latitude. *J. Atmos. Solar-Terr. Phys.*, *71*(17-18), 1943–1947. https://doi.org/10.1016/j.jastp.2009.08.004

Thébault, E., Finlay, C. C., Beggan, C. D., Alken, P., Aubert, J., Barrois, O., Bertrand, F., Bondar, T., Boness, A., Brocco, L., and Zvereva, T. (2015). International geomagnetic reference field: the 12th generation. *Earth Planets Space*, *67*(1), 79. https://doi.org/10.1186/s40623-015-0228-9

Woodman, R. F., Yamamoto, M., and Fukao, S. (1991). Gravity wave modulation of gradient drift instabilities in mid-latitude sporadic *E* irregularities. *Geophys. Res. Lett.*, *18*(7), 1197–1200. https://doi.org/10.1029/91GL01159

Wu, J. N., Zhou, C., Wang, G., Liu, Y., Jiang, C. W., and Zhao, Z. Y. (2022). Simulation of E_s layer modulated by nonlinear Kelvin–Helmholtz instability. *J. Geophys. Res.: Space Phys.*, *127*(8), e2021JA030065. https://doi.org/10.1029/2021JA030065

Yamazaki, Y., Arras, C., Andoh, S., Miyoshi, Y., Shinagawa, H., Harding, B. J., Englert, C. R., Immel, T. J., Sobhkhiz-Miandehi, S., and Stolle, C. (2022). Examining the wind shear theory of sporadic E with ICON/MIGHTI winds and COSMIC-2 radio occultation data. *Geophys. Res. Lett.*, *49*(1), e2021GL096202. https://doi.org/10.1029/2021GL096202

Yu, B. K., Xue, X. H., Yue, X. A., Yang, C. Y., Yu, C., Dou, X. K., Ning, B. Q., and Hu, L. H. (2019). The global climatology of the intensity of the ionospheric sporadic *E* layer. *Atmos. Chem. Phys.*, *19*(6), 4139–4151. https://doi.org/10.5194/acp-19-4139-2019

Yu, B. K., Scott, C. J., Xue, X. H., Yue, X. A., and Dou, X. K. (2020). Derivation of global ionospheric Sporadic E critical frequency (f_oE_s) data from the amplitude variations in GPS/GNSS radio occultations. *Roy. Soc. Open Sci.*, *7*(7), 200320. https://doi.org/10.1098/rsos.200320

Yue, X. A., Wan, W. X., Ning, B. Q., and Jin, L. (2022a). An active phased array radar in China. *Nat. Astron.*, *6*(5), 619. https://doi.org/10.1038/s41550-022-01684-1

Yue, X. A., Wan, W. X., Ning, B. Q., Jin, L., Ding, F., Zhao, B. Q., Zeng, L. Q., Ke, C. H., Deng, X. H., … Liu, F. Y. (2022b). Development of the Sanya incoherent scatter radar and preliminary results. *J. Geophys. Res.: Space Phys.*, *127*(8), e2022JA030451. https://doi.org/10.1029/2022JA030451

Yue, X. A., W. Schreiner, S., Pedatella, N. M., and Kuo, Y-H. (2016). Characterizing GPS radio occultation loss of lock due to ionospheric weather. *Space Weather*, *14*(4), 285–299, https://doi.org/10.1002/2015SW001340

Zhang, B. Z., Sorathia, K. A., Lyon, J. G., Merkin, V. G., Garretson, J. S., and Wiltberger, M. (2019). GAMERA: a three-dimensional finite-volume MHD solver for non-orthogonal curvilinear geometries. *Astrophys. J. - Suppl. Ser.*, *244*(1), 20. https://doi.org/10.3847/1538-4365/ab3a4c

Zhou, X., Yue, X. A., Wang, J. Y., Cai, Y. H., Ding, F., Ning, B. Q., Jin, Y. Y., Li, M. Y., Wang, Y. H., … Luo, J. H. (2023). "Ionospheric drizzle" observed in the pre-dawn E-F valley over Sanya. *J. Geophys. Res.: Space Phys.*, *128*(6), e2023JA031481. https://doi.org/10.1029/2023JA031481

Zuo, X. M., Wan, W. X., and Tan, H. (2006). Observational evidences and simulation of tide wind induced mid-latitude sporadic E-layers. *Chin. J. Space Sci. (in Chinese)*, *26*(5), 346–351. https://doi.org/10.11728/cjss2006.05.346